

Article

Novel Bi-Functional MoS₂/α-Fe₂O₃ Nanocomposites for High Photocatalytic Performance

Islam Ibrahim ^{1,2,3} , Pinelopi P. Falara ^{1,4}, Elias Sakellis ¹ , Maria Antoniadou ⁵, Chrysoula Athanasekou ¹ and Michalis K. Arfanis ^{1,*} 

¹ Institute of Nanoscience and Nanotechnology, National Centre for Scientific Research (NCSR) “Demokritos”, Agia Paraskevi, 15341 Athens, Greece; i.ibrahim@inn.demokritos.gr (I.I.); pin.falara@gmail.com (P.P.F.); e.sakellis@inn.demokritos.gr (E.S.); c.athanasekou@inn.demokritos.gr (C.A.)

² Department of Chemistry and Biochemistry, Florida International University, Miami, FL 33199, USA

³ Department of Chemistry, Faculty of Science, Al-Azhar University, Nasr City, Cairo 11884, Egypt

⁴ School of Chemical Engineering, National Technical University of Athens, Zografos Campus, 15773 Athens, Greece

⁵ Department of Chemical Engineering, University of Western Macedonia, 51000 Kozani, Greece; mantoniadou@uowm.gr

* Correspondence: m.arfanis@inn.demokritos.gr; Tel.: +30-21-0650-3668

Abstract: In this study, 3-dimensional molybdenum disulfide (MoS₂) structures, integrated with hematite (α-Fe₂O₃) nanoparticles, were fabricated under a convenient two-step hydrothermal route. The fabricated photocatalytic nanocomposites consist of well-arranged MoS₂ flakes, resembling spherical flower-like morphology, and the nanoparticulate α-Fe₂O₃ structures decorate the 3D network. By raising the α-Fe₂O₃ weight ratio, the composites’ specific surface area and morphology were not affected, regardless of the partial cover of the cavities for higher hematite content. Moreover, the crystallinity examination with XRD, Raman, and FTIR techniques revealed that the precursor reagents were fully transformed to well-crystallized MoS₂ and Fe₂O₃ composites of high purity, as no organic or inorganic residues could be detected. The photocatalytic oxidation and reduction performance of these composites was evaluated against the tetracycline pharmaceutical and the industrial pollutant hexavalent chromium, respectively. The improvement in the removal efficiencies demonstrates that the superior photoactivity originates from the high crystallinity and homogeneity of the composite, in combination with the enhanced charge carriers’ separation in the semiconductors’ interface.

Keywords: MoS₂; α-Fe₂O₃; photocatalysis; tetracycline oxidation; Cr⁶⁺ reduction



Citation: Ibrahim, I.; Falara, P.P.; Sakellis, E.; Antoniadou, M.; Athanasekou, C.; Arfanis, M.K. Novel Bi-Functional MoS₂/α-Fe₂O₃ Nanocomposites for High Photocatalytic Performance. *ChemEngineering* **2024**, *8*, 20. <https://doi.org/10.3390/chemengineering8010020>

Academic Editor: Ilenia Rossetti

Received: 16 December 2023

Revised: 11 January 2024

Accepted: 1 February 2024

Published: 6 February 2024



Copyright: © 2024 by the authors. Licensee MDPI, Basel, Switzerland. This article is an open access article distributed under the terms and conditions of the Creative Commons Attribution (CC BY) license (<https://creativecommons.org/licenses/by/4.0/>).

1. Introduction

Nowadays, the maintenance of freshwater quality and wastewater management are highly related to the efficient operation of municipal water treatment plants (MWTPs). At the moment, recalcitrant substances like pharmaceuticals, pesticides, personal care products, or different types of organic and inorganic industrial pollutants are insufficiently eliminated at MWTPs; therefore, additional procedures should be adopted. Among the proposed approaches, the integration of the existing water treatment technologies with photocatalytic advanced oxidation processes (AOPs) gain significant impact because of their simplicity and effectiveness [1,2]. In this regard, photocatalysis takes the advantage of semiconductors’ photoexcitation with solar light and their ability to create reactive oxidative species (ROS), which are able to destroy organic and inorganic contaminants of emerging concern [3]. The activity of the photocatalytic materials can be evaluated against a variety of contaminants, such as tetracycline, an antibiotic for bacterial infections in both human and animals [4]; nitenpyram, an insecticide toxin based on neonicotinoid compound [5]; *p*-nitrophenol, a poisonous precursor of the chemical industry [6]; chlorobenzene and toluene, a representative polluting gas mixture of aromatic volatile organic compounds [7];

hexavalent chromium, a commonly used heavy metal in industrial manufacturing of pigments and anti-corrosion protection [8]; or even the inhibition of *Staphylococcus aureus* and *Escherichia coli* bacteria [9].

During the recent years, titanium dioxide was extensively studied in wastewater treatment applications and was established as the most efficient photocatalyst; however, it cannot exploit the whole range of solar light and its quantum efficiency is limited due to recombination effects [1]. The fabrication of alternative nanomaterials or nanocomposites, instead of TiO_2 , could be a feasible strategy to improve the impact of photocatalytic processes as a reliable choice for wastewater management. Molybdenum disulfide (MoS_2) could be an ideal candidate due to its advanced optoelectronic properties [10], while its layered morphology provides higher surface area, which enhances the adsorption and degradation of the target compounds [11]. However, most often, MoS_2 is packed on multi-layered aggregates, leading to a lower number of active sites, lower charge carriers' mobility, and a lower photocatalytic performance [12]. In order to overcome the intrinsic limitations of MoS_2 , the combination with other catalysts, like iron oxides, and the development of composites is suggested [10,13].

Recently, the fabrication and the performance of MoS_2 composites with hematite ($\alpha\text{-Fe}_2\text{O}_3$) was taken into consideration because the hematite's energy band levels match with the respective levels of MoS_2 , enabling band alignment and enhancing charge carrier separation [14]. Moreover, hematite is a well-known photocatalyst with a relatively short energy gap and it is earth abundant and eco-friendly [15]. Depending on the experimental conditions, $\alpha\text{-Fe}_2\text{O}_3$ has the ability to decompose contaminants through the production of reactive radicals based on heterogeneous photocatalysis and/or the Fenton mechanism [16,17]. Interestingly, the $\text{MoS}_2/\text{Fe}_2\text{O}_3$ composites are not examined thoroughly, regardless of their superior opto-electronic properties, which imply improved photocatalytic performance. Occasionally, some studies of $\text{MoS}_2/\alpha\text{-Fe}_2\text{O}_3$ materials focus on their photoelectrochemical properties and their utilization in supercapacitors [18], water splitting systems [19], or the photo-electro-catalytic degradation of pollutants [20]. Additionally, the evolution of oxygen [21], or the production of photofuels, like H_2 production and hydrocarbons [22,23], has been reported. Nevertheless, applications on the photocatalytic degradation of emerging contaminants is limited on the elimination of organic dyes, such as methylene blue and rhodamine-B [24,25], while the examination of recalcitrant and persistent organic pollutants in water, like pharmaceuticals [26], is generally missing. In addition, most of these studies fabricate ternary composites, by coupling the binary $\text{MoS}_2/\alpha\text{-Fe}_2\text{O}_3$ systems with other semiconductors or graphitic materials [19,25]. On the other hand, some studies explore binary systems using different ferrite phases, but they cannot exclude the formation of additional intrinsic impurities [13].

Herein, $\text{MoS}_2/\text{Fe}_2\text{O}_3$ heterostructures (noted as MoFe) were synthesized under a two-step hydrothermal method and their morphological, spectroscopic, and photocatalytic properties were examined in depth. Compared to the existing reports for $\text{MoS}_2/\text{Fe}_2\text{O}_3$ fabrication under hydrothermal or other wet chemistry approaches, in this study, the excess of thiourea was adjusted appropriately regarding the molarity of molybdenum precursors, while the added hematite quantities were used to prepare MoFe-nanostructured composites with 1:2, 1:1, and 2:1 weight ratios of the individual materials. Under this synthetic route, MoS_2 flakes were packed in an extended 3D flower-like network, free from any undesired crystal phases or impurities, and were decorated with well-dispersed nanoparticulate $\alpha\text{-Fe}_2\text{O}_3$ crystals. In addition, the photo oxidation of the tetracycline pharmaceutical and the photoreduction of hexavalent chromium with MoFe was rarely examined under the applied conditions. In particular, the experiments occurred in the absence of hydrogen peroxide (H_2O_2) additives in order to prevent the direct activation of the Fenton mechanism; therefore, only photocatalytic reactions occurred and were evaluated.

2. Materials and Methods

2.1. Materials Synthesis

In order to prepare hematite (α -Fe₂O₃) nanoparticles, 5.05 g ferric nitrate (Fe(NO₃)₃•9H₂O) was dispersed in a 25 mL ethanol/125 mL DI H₂O mixture. Then, 10 g sodium acetate (CH₃COONa) was added to the above solution and stirred for 30 min. Subsequently, the hydrothermal treatment was performed at 180 °C for 24 h. The final oxide was obtained after several washing cycles with DI water and was dried at 50 °C overnight [27].

The preparation of MoS₂ nanopowders was also based on a one-step hydrothermal method [28]. In brief, 0.525 g of ammonium molybdate tetrahydrate (NH₄6Mo₇O₂₄•4H₂O) was mixed with 0.455 g of sulfur precursor (thiourea, H₂CSNH₂) in 125 mL DI water and stirred for 90 min, in order to adjust their molar ratio to ~1:15. The resultant solution was placed into a 300 mL autoclave and kept there for 24 h at 200 °C. The black precipitate was washed multiple times with DI water and absolute ethanol, and was finally dried overnight at 80 °C. Following this technique, ~160 mg of pure MoS₂ was obtained.

Finally, the nanocomposites were prepared by mixing hematite in a MoS₂ precursor solution. The α -Fe₂O₃ content was adjusted to 80, 160, or 320 mg, assuming that the weight ratios between α -Fe₂O₃ and MoS₂ would approximate to 2:1, 1:1, and 1:2 after the hydrothermal process. Before hydrothermal treatment, mixture homogenization was established under 1 h sonication and stirring for half an hour. Following the same annealing, washing, and drying steps, the derived samples were named as MoFe (2:1), MoFe (1:1), and MoFe (1:2)—regarding the relative weight ratio of the two catalysts.

2.2. Materials Characterization

The diffractometer Siemens D-500 with Cu K α 1 ($\lambda = 1.5406 \text{ \AA}$) and Cu K α 2 ($\lambda = 1.5444 \text{ \AA}$) was used to carry out X-ray powder diffraction (XRPD) analyses for all prepared nanocomposites (Siemens, Erlangen, Germany). The data were collected for 3 s at 0.02° increments in detector placement in the range of $5^\circ \leq 2\theta \leq 80^\circ$.

The micro-Raman spectra were performed with a Renishaw reflex spectrometer (Renishaw, Wotton-under-Edgr, UK) using diode laser beams at $\lambda = 514.5 \text{ nm}$ and 785 nm. Each laser beam was directed on the prepared catalysts using a $\times 50$ objective, with power density equal to $0.02 \text{ mW } \mu\text{m}^{-2}$. The scattered light was collected by an ultra-highly sensitive CCD detector.

Fourier transform infrared (FTIR) spectra were acquired using a Thermo Scientific Nicolet 6700 FTIR under N₂ flow (Thermo Scientific, Pittsburgh, PA, USA). Spectra were obtained utilizing a transmission cell containing a potassium bromide pellet. Data were obtained between 4000 and 400 cm⁻¹ (with a resolution of 4 cm⁻¹).

By using barium sulfate as a reference, the optical characteristics of the samples were examined using a UV-Vis diffuse reflectance spectrometer Hitachi 3010 (Hitachi, Tokyo, Japan), equipped with an integrating sphere (60 mm diameter).

The morphological properties of the prepared samples were collected using a Philips Quanta FEI Inspect Scanning Electron Microscope (SEM, FEI company, Eindhoven, The Netherlands) by employing a tungsten filament running at 25 keV. The morphology of the nanostructure was studied using a high-resolution FEI Talos F200-i field emission (scanning) transmission electron microscope (S/TEM) operating at 200 kV. The microscope (Thermo Fisher Scientific Inc., Waltham, MA, USA) was equipped with a windowless energy-dispersive spectroscopy microanalyzer (6T/100 Bruker, Hamburg, Germany). In all cases, approximately 0.2 g of each sample was received, and the powders were suspended in alcohol, followed by ultrasonication in order to reduce possible agglomeration of the nanoparticles. Subsequently, a drop from the resulting suspension was deposited on a 300-mesh carbon coated copper grid and was air-dried overnight. The S/TEM was also equipped with an Oxford X-Max 100 Silicon Drift Energy-Dispersive X-ray (EDX) Spectrometer (Oxford Instruments, Wycombe, UK), with a probe size varying between 2 and 5 nm. Therefore, both elemental and mapping analyses were performed via EDX.

The textural characteristics of the samples were evaluated by N₂ adsorption–desorption isotherms at $-196\text{ }^{\circ}\text{C}$, using an automated volumetric system (Autosorb-ASiQ, Quantachrome, Boynton Beach, FL, USA). Prior to each measurement, the samples were degassed at $200\text{ }^{\circ}\text{C}$ for 48 h under high vacuum, which was achieved with a turbomolecular pump. The specific surface area was estimated using the Brunauer–Emmett–Teller (BET) equation. Similarly, the volume and cumulative surface area of the mesopores were calculated via the Barrett–Joyner–Halenda (BJH) method.

The electrochemical characterization of the samples was conducted with an Autolab PGSTAT-30 potentiostat (Metrohm/Eco Chemie, Utrecht, The Netherlands) under simulated solar light (1 sun, $1000\text{ W}\cdot\text{m}^{-2}$) from a Xenon lamp combined with AM 1.5G optical filters. Nyquist plots were obtained using a standard 3-electrode system; a platinum foil (Pt) as a counter electrode; and a silver/silver chloride (Ag/AgCl) with electrolyte concentration $C_{\text{KCl}} = 3\text{ M}$ as a reference electrode. The working electrode was produced as follows: 5 mg of the photocatalyst was dispersed into a solution comprising 25 μL Nafion perfluorinated, 145 μL 3D water, and 84 μL absolute ethanol. The above solution was ultrasonicated for 2 h in order to obtain uniform suspension. Following this, a doctor blade technique was utilized to fabricate a uniform 1 cm^2 active area on a clean FTO electrode. The sample was then annealed at $450\text{ }^{\circ}\text{C}$. The solution used for the electrochemical measurements contained a sodium sulfate (Na_2SO_4) electrolyte with a concentration of 0.2 M [29].

2.3. Photocatalytic Experiments

Lastly, the photocatalytic properties of the fabricated samples were evaluated during the photo oxidation of the tetracycline pharmaceutical (TC) and the photoreduction of the hexavalent chromium (Cr(IV)) industrial pollutant. In brief, the photocatalytic performance of MoS_2 , Fe_2O_3 , and $\text{MoS}_2/\text{Fe}_2\text{O}_3$ nanocomposites was investigated under UV light by suspending 5 mg of each catalyst in 50 mL of Cr^{6+} solution (5 ppm) and adding 6 drops of 0.2 M H_2SO_4 . The solution was stirred in the dark for 10 h to achieve an adsorption–desorption equilibrium. UV irradiation was performed using a black box photoreactor ($50\text{ cm} \times 50\text{ cm} \times 30\text{ cm}$), connected with four UV-A, 4-Sylvania TLD 15 W/08 lamps (350–390 nm, $0.23\text{ mW}/\text{cm}^2$, Feilo Sylvania, Erlangen, Germany). The photoreduction process was evaluated using a colorimetric method with a diphenylcarbazine metal ion indicator and by measuring the absorbance of the Cr^{6+} –diphenylcarbazide complex (542 nm) at equal time intervals. In the case of tetracycline photo oxidation, 0.2 g/L of the samples was suspended in 10 mL of TC solution (20 ppm). After reaching the adsorption–desorption equilibrium (lasted 60 min), the catalysts were separated from the suspension (6000 rpm, EBA 2000, Hettich, Tuttlingen, Germany) and the characteristic absorption peak of TC at 357 nm was determined.

3. Results

3.1. Morphology Characterization

First, the morphological examination of the MoS_2 , $\alpha\text{-Fe}_2\text{O}_3$, and MoFe samples was performed with SEM microscopy (Figures 1 and S1). The MoS_2 nanoparticles consist of multi-layered flakes, a thickness of $\sim 20\text{ nm}$, and a length ranging from 180 to 300 nm. These flakes are clustered to bigger and well-arranged spherical formations, resembling 3D flower-like structures, with an average diameter of 2.2 μm . Upon the addition of different amounts of hematite, the hematite-rich MoFe (1:1) and MoFe (1:2) samples maintained their flower-like structures, although the spheres considerably shrank and the empty spaces among the flakes were partially filled. On the contrary, the flakes in the MoS_2 -rich MoFe (2:1) samples were curved and filled the voids of the flower, without affecting the size and shape of the spherical structure. Interestingly, even if the pristine hematite nanoparticles form micro-sized bulk aggregates (Figure S1a,b), this tendency is not observed in the case of the MoFe samples. Probably, upon the addition of the pre-synthesized $\alpha\text{-Fe}_2\text{O}_3$ in the MoS_2 precursor solution, the oxide is either fragmented or dispersed uniformly along the flakes

of the sulfide photocatalyst during the hydrothermal process, or it acts as a condensation core for the sulfide [23].

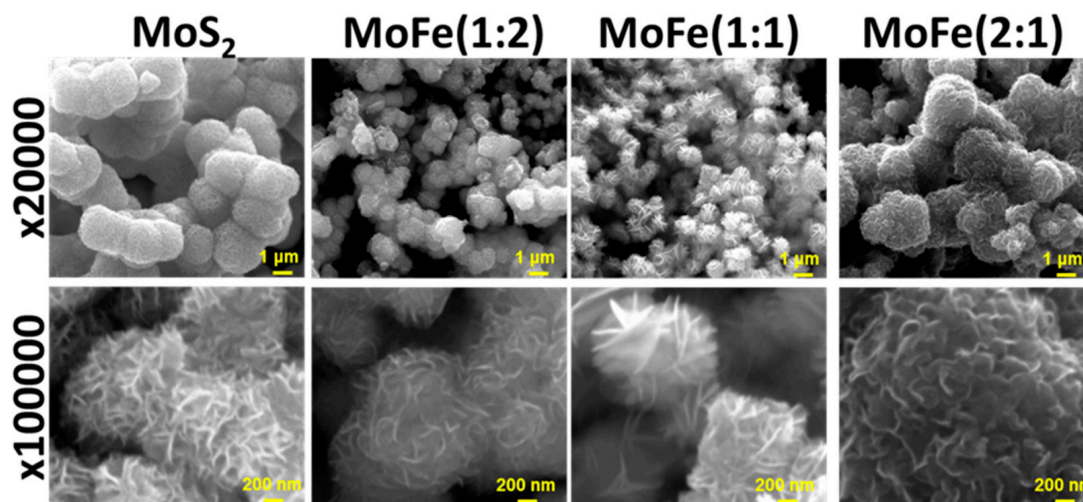


Figure 1. SEM images of MoS₂ and MoFe nanoparticles in ×20,000 and ×100,000 magnification.

Next, TEM images were captured, as shown in Figure 2, in order to investigate the morphology and the structural features of the as-synthesized MoS₂, α-Fe₂O₃, and MoFe (2:1) samples. Figure 2a clearly shows that MoS₂ flakes are condensed, creating a 3D flower-like structure. The higher magnification for the MoS₂-layered structure (Figure 2b) reveals that the interspace distance of the crystal lattice is approximately 0.615 nm, corresponding to the (002) plane of hexagonal MoS₂. The hexagonal crystal structure of α-Fe₂O₃ is evident in Figure 2c, in which the lattice spacing of the (110) crystallographic planes is calculated to be 0.25 nm (Figure 2d). In the case of the MoFe (2:1) sample, the oxide's domains are not evident (Figure 2e). Nevertheless, the MoFe (2:1) composite's elemental mapping images (Figure S2) reveal the co-presence of Fe with Mo, O, and S elements in the selected area, verifying the successful preparation of the MoS₂/α-Fe₂O₃ nanocomposite. Possibly, the iron oxide was condensed into the structures of lower dimensions (unable to be observed with SEM or TEM), achieving a complete coverage of MoS₂ flakes during the second hydrothermal treatment step.

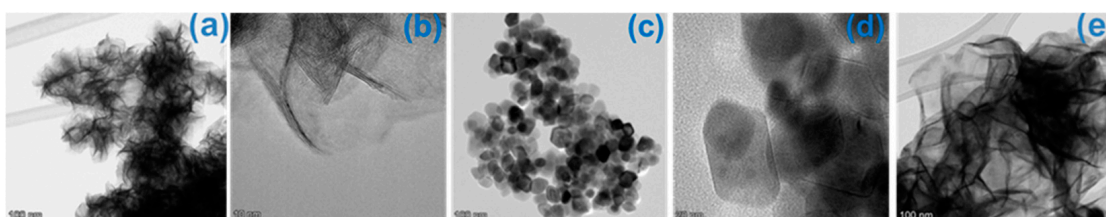


Figure 2. HR-TEM of MoS₂ (a,b), α-Fe₂O₃ (c,d), and MoFe (2:1) (e) in different magnifications.

In order to explore the textural properties of the composites, N₂ porosimetry experiments took place for the MoS₂-based samples (Figure S4). The N₂ adsorption–desorption isotherms present typical type IV isotherms with H3 hysteresis, corresponding to mesoporous material as indicated by the IUPAC classification. All samples have mesopores with diameter in the range of 2–50 nm, whereas the MoFe (2:1) and MoFe (1:2) composites also exhibit macropores in the range of 50 to 350 nm. As shown in Table 1, BET surface area values of all composites have a slightly lower surface area and pore size than the initial MoS₂ sample. Accordingly, the hematite's BET is more than double that of the MoFe (1:2) and MoFe (2:1) samples' and almost double that of the MoFe (1:1) and MoS₂ samples'. Moreover, the hematite sample shows the highest total pore volume value. These observations show that the values of the composites are slighter than the pristine MoS₂,

and they support the fact that the nanoparticulate hematite covers the MoS₂ surface during hydrothermal treatment, leading to blocked pores and limited BET surface area.

Table 1. Textural properties of the prepared photocatalysts.

	α -Fe ₂ O ₃	MoS ₂	MoFe (1:2)	MoFe (1:1)	MoFe (2:1)
BET surface area (m ² /g)	70.0	39.5	27.5	37.8	28.8
Total pore volume (cm ³ /g)	0.185	0.120	0.104	0.134	0.093

3.2. Structural Characterization

The XRD patterns of the synthesized MoS₂, α -Fe₂O₃, and MoFe nanocomposites are presented in Figure 3. Starting with the XRD pattern of MoS₂, diffractions are shown as peaks at $2\theta = 14.37^\circ$, 33.5° , 39.53° , and 58.33° , which correspond to the (002), (100), (103), and (110) crystal planes of hexagonal MoS₂ (pdf 24-0513), respectively. Next, the pattern of the α -Fe₂O₃ nanoparticles reveals the characteristic diffractions of (012), (104), (110), (113), (024), (116), (122), (214), and (300) at $2\theta = 24.13^\circ$, 33.15° , 35.61° , 40.85° , 49.47° , 54.08° , 57.42° , 62.44° , and 63.98° , respectively, which are assigned to the standard pure hexagonal hematite (pdf 24-0072). All these crystallographic findings are in agreement with the TEM analysis, confirming the main crystal system and crystal planes of each material. Last, the XRD patterns of the nanocomposites indicate that the formed MoS₂ nanoparticles were successfully incorporated with the α -Fe₂O₃ materials, as the diffractions of both α -Fe₂O₃ and MoS₂ co-exist in the composites patterns. In particular, hematite diffractions are always present in these composites' patterns, although the oxide diffraction was more intense in the case of the α -Fe₂O₃-rich MoFe (1:2) sample.

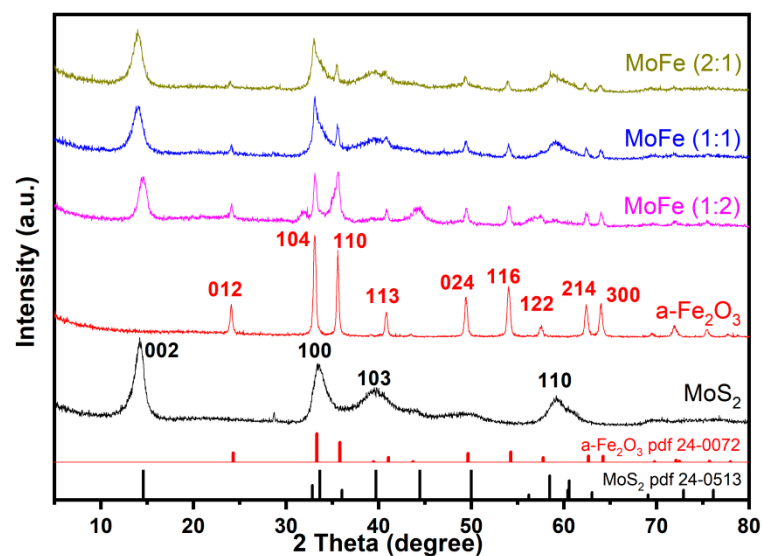


Figure 3. XRD patterns of MoS₂, α -Fe₂O₃, and MoFe nanoparticles.

The examination with vibrational Raman spectroscopy also confirmed the successful fabrication of molybdenum disulfide and hematite (Figure 4). First, the acquired spectrum of MoS₂ revealed a typical fingerprint of hexagonal 2H MoS₂ materials: the in-plane E_{2g} band of two S atoms vibrated in the opposite direction in respect to the Mo atom (381 cm^{-1}) and the out-of-plane A_{1g} band of the of S atoms along the c axis (407 cm^{-1}) [30]. Interestingly, the frequency difference between the two bands exceeds 20 cm^{-1} , suggesting that sulfide is multi-layered [31]. Moreover, the E_{1g} band at 286 cm^{-1} is Raman-active in bulk 2H MoS₂ materials, providing more evidence for the bulk nature of the material [32]. On the other hand, the presence of a longitudinal acoustic phonon mode at 224 cm^{-1} and its resonance enhanced overtone at 457 cm^{-1} might correspond to lattice disorders or structural changes, which are related to the co-existence of the octahedral T1 MoS₂

phase [32,33]. The analysis of the hematite presented characteristic vibration A_{1g} bands at 224 and 499 cm^{-1} (related to octahedral $\text{Fe}(\text{O})_6$ motions), and E_g bands at 244, 294–298 (double mode), 409, and 412 cm^{-1} (related to the rotations and translations of the Fe_2O_3 lattice), and displayed a longitudinal optical phonon (LO) at 661 cm^{-1} [34]. Regarding the MoFe composites, their diagrams did not have significant differences compared to the pristine MoS_2 because the Fe–O modes were absent. The only indirect proof of the semiconductors' incorporation was the slight redshifts of the E_{2g} band and the blueshifts of A_{2g} , which are associated with the coupling of MoS_2 with oxide [35]. Nevertheless, some random aggregates were detected in the case of the $\alpha\text{-Fe}_2\text{O}_3$ -rich samples comprising MoFe (1:1) and MoFe (1:2), in which localized $\alpha\text{-Fe}_2\text{O}_3$ formations could be identified (Figure S3a,b). The extent and size of these formations were more easily detected across the MoFe (1:2) samples. These spectroscopic observations are in accordance with the morphological findings, as long as the 2H bulk MoS_2 is mainly identified on the surface and the $\alpha\text{-Fe}_2\text{O}_3$ vibrations are not detected, and when either the hematite is nano-sized or well-distributed across the sulfide, or when it is located in the internal part of the MoFe structures.

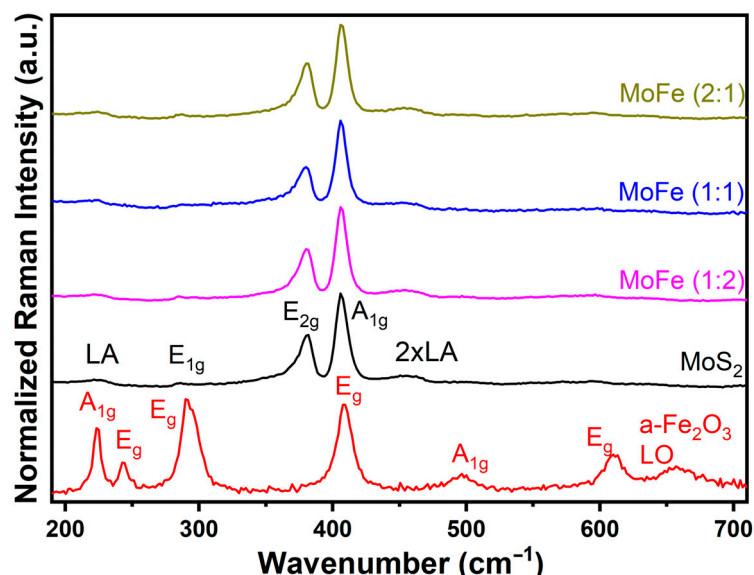


Figure 4. Raman spectra of $\alpha\text{-Fe}_2\text{O}_3$, MoS_2 , and MoFe nanoparticles.

Figure 5 shows the FTIR spectra of as-synthesized MoS_2 , $\alpha\text{-Fe}_2\text{O}_3$, and MoFe nanocomposites. In general, molybdenum disulfide crystals might present a very weak Mo–S vibration mode at the skeletal region; therefore, its absence at $\sim 600 \text{ cm}^{-1}$ does not affect the materials' evaluation [36]. However, it is remarkable that neither covalent bonds of carbon with C, N, O, and/or H, nor the sulfur complexes, were observed at the skeletal and the functional group regions [36], implying that thiourea was totally consumed during the hydrothermal process and pure MoS_2 was formed. In the case of the $\alpha\text{-Fe}_2\text{O}_3$ nanoparticle, the presence of Fe_2O_3 was confirmed with two dominant bands at 470 and 540 cm^{-1} , which are related to metal–oxygen stretching vibrations (Fe–O) [37]. These bands were also present in all MoFe samples, especially in the Fe-rich composite.

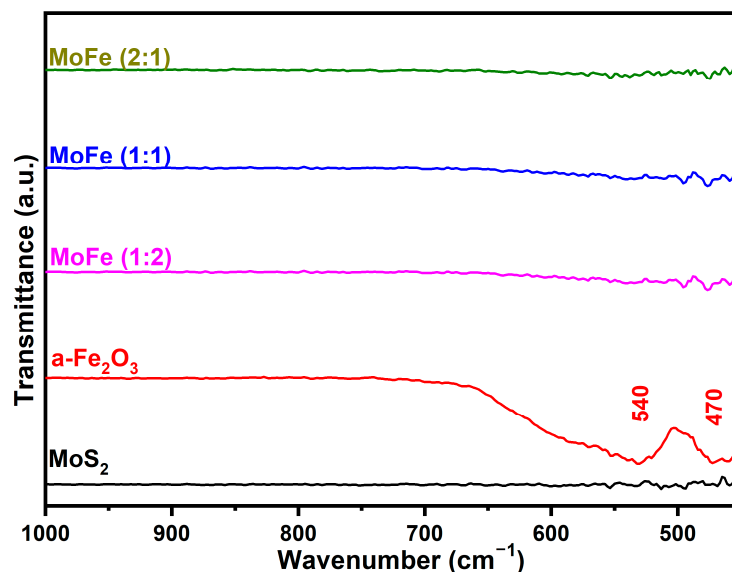


Figure 5. IR spectra of the prepared photocatalysts.

3.3. Optoelectronic Properties

Concerning the optical properties and the estimated band gaps of the synthesized composite, it should be first mentioned that the MoS₂ band gap is correlated with the material's morphology. In particular, if MoS₂ is synthesized in the form of a monolayer, then the respective band gap is direct, while multilayered MoS₂ structures have indirect gaps [10,11]. Based on the SEM images, it is apparent that the flower-like structures consist of aggregated MoS₂ thin flakes, so both band gap types could be expected in all samples. Indeed, the obtained absorption spectra in Figure 6, expressed in Kubelka–Munk units (F(R)), reveal that two intense peaks in the regions of 300–400 nm and 500–600 nm co-exist and are attributed to the indirect and direct transitions of the photo-charge carriers [38]. On the other hand, the reference hematite material presented a typical absorbance spectrum, where both O_{2p} → Fe_{3d} (~400 nm) and Fe_{3d} → Fe_{3d} (~540 nm) transitions were detected [39].

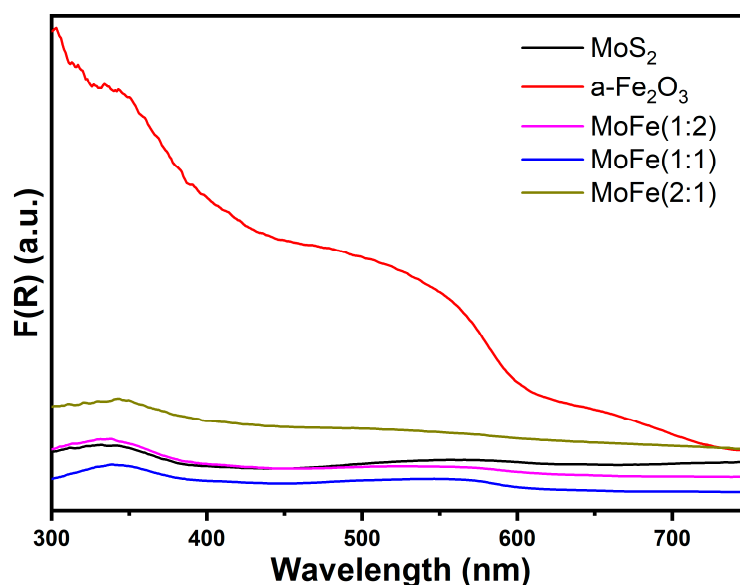


Figure 6. Absorbance spectra of α -Fe₂O₃, MoS₂, and MoFe nanoparticles, expressed in Kubelka–Munk units.

Next, the acquired Nyquist plots from impedance spectroscopy (Figure 7) provide insights into the charge transfer resistance of the photoexcited electron–hole pairs. The

shorter semicircle diameters of the composite materials demonstrate that the incorporation of α -Fe₂O₃ with MoS₂ improves the charge carriers' separation and limits the recombination effects [29]. Even if there is no specific tendency between the oxide quantity in the composites and reduced resistance, an obvious improvement is observed; therefore, the enhanced generation of reactive radicals is also predicted during photocatalysis compared to the reference molybdenum disulfide sample.

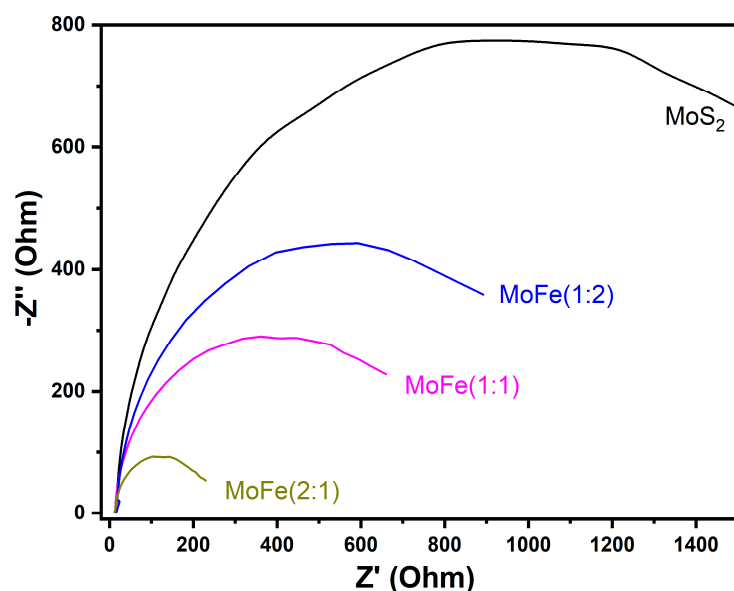


Figure 7. Nyquist plots of the reference MoS₂ and MoFe samples.

3.4. Photocatalytic Performance

The photocatalytic performance of the synthesized samples was examined with a tetracycline pharmaceutical and hexavalent chromium industrial additive in order to investigate the materials' performance on oxidation and reduction mechanism pathways, respectively. Starting with TC (Figure 8a), the ferrite was totally inactive, implying that neither adsorption nor photocatalytic and Fenton reactions take place. Similarly, the MoS₂ reference material presented poor removal activity after reaching the adsorption-desorption equilibrium of ~80%. On the other hand, the TC photodegradation with MoFe composites improved remarkably; the TC concentration decreased to 40% with MoFe (2:1) after 3 h of UV illumination, 55% with MoFe (2:1), and 62% with MoFe (1:2). This trend must be related to the interaction of hematite with the MoS₂ because the Fenton reactions cannot be activated under experimental conditions; hydrogen peroxide additives were not used as solutions during UV irradiation, while the photocatalytic generation of H₂O₂ for Fe₂O₃/MoS₂ systems has been already excluded from previous studies [40]. Based on this investigation, the optoelectronic properties of the composites and the existence of localized α -Fe₂O₃ formations are the most important factors in photocatalysis. First, the charge transfer resistance of the samples is in line with the photodegradation rates of TC, suggesting that the samples' efficacy to separate photo-charged carriers has resulted in an enhanced generation of ROS. Moreover, the simultaneous presence of both direct and indirect energy gaps on the MoS₂ samples increases the materials' responses during incident illumination, producing higher numbers of ROS [38]. Interestingly, MoFe (2:1) was the only sample without any α -Fe₂O₃ impurities across its surface, implying that the material's purity is related to its enhanced photocatalytic efficiency. On the contrary, MoFe (1:1) and MoFe (1:2) contain α -Fe₂O₃ impurities all across their surface, which are able to affect e⁻/h⁺ separation, ROS production, and their photocatalytic performance.

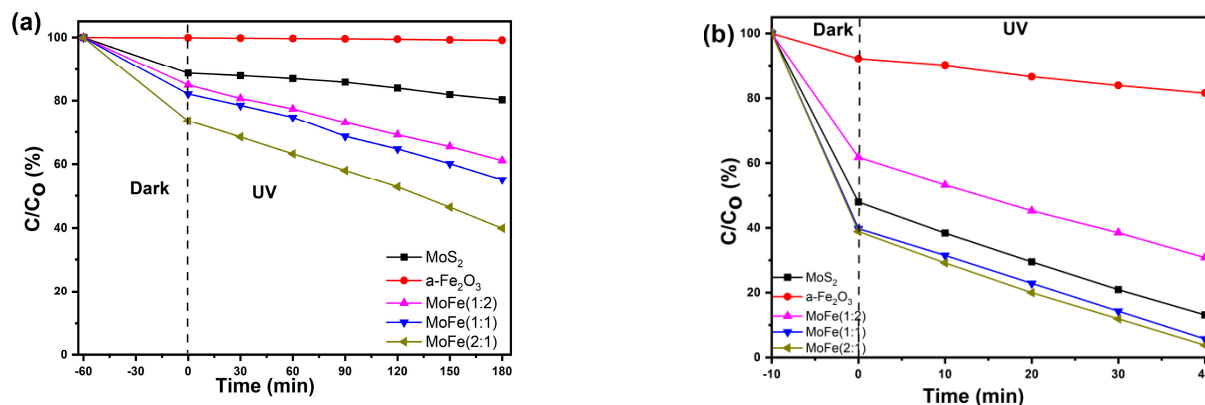


Figure 8. Photocatalytic oxidation of tetracycline (a) and reduction of hexavalent Cr (b) with α -Fe₂O₃, MoS₂, and the MoFe composites.

Concerning the photocatalytic conversion of Cr(VI) to a trivalent with MoFe materials, the findings are in accordance with the above-mentioned results (Figure 8b). In particular, MoFe (2:1) was the best photocatalyst, reaching an almost 100% hexavalent chromium reduction, while MoFe (1:2) presented poor activity, which was close to 30%. Compared to the reference MoS₂ sample, the MoFe composites performed equally well, implying that the incorporation of α -Fe₂O₃ did not alter the photoreduction yields. In particular, the deterioration of Cr(VI) photoreduction with MoFe samples should be expected because the addition of hematite lessens the composites' specific surface area and the pore volume, compared to the reference MoS₂ [12]. Nevertheless, the composites' effectiveness was maintained close to the reference material. Raman analysis and impedance spectroscopy implied that crystallinity and e⁻/h⁺ separation may have a higher impact in photocatalysis compared to SSA, meaning that the improved optoelectronic properties have balanced the SSA decrement.

4. Conclusions

The results of this study established the efficient incorporation and fabrication of photocatalytic MoS₂/ α -Fe₂O₃ composites (noted as MoFe) under a convenient two-step hydrothermal route. The formed flakes of the hexagonal molybdenum disulfide were packed in an extended 3D flower-like network, which was decorated with well-dispersed nanoparticulate α -Fe₂O₃ crystals. The alteration of the precursors' ratio during synthesis influenced the morphology, surface area, and charge transfer resistance of the produced MoFe samples, while the structural and optical properties remained intact. Remarkably, the two-step synthesis process produced homogeneous materials, especially in the case of the MoFe(2:1) sample, as no organic or inorganic impurity domains were detected during the examination with vibrational spectroscopic techniques. The photocatalytic activity of the synthesized composites revealed that MoFe (2:1) achieved 60% removal for the tetracycline pharmaceutical and complete removal of the hexavalent chromium industrial additive, suggesting that the material's high purity and the limited recombination of the photogenerated charge carriers are the key parameters for its superior performance.

Supplementary Materials: The following supporting information can be downloaded at: <https://www.mdpi.com/article/10.3390/chemengineering8010020/s1>, Figure S1: SEM images of hematite in $\times 20,000$ (a) and $\times 50,000$ (b) magnification; Figure S2: HAADF-STEM image of MoFe (2:1) (a) and the corresponding elemental mapping images of Fe K-edge (b; blue), Mo K-edge (c; red), and S K-edge (d; green); Figure S3: Raman examination of MoFe (1:1) (a) and MoFe (1:2) (b) at different spots across their surface; Figure S4: N₂ adsorption–desorption isotherms (a,c,e,g,i) and pore size distribution (b,d,f,h,j) curves of the prepared photocatalysts.

Author Contributions: Conceptualization, I.I. and M.K.A.; validation and methodology, I.I., P.P.F., E.S., M.A., C.A. and M.K.A.; investigation and writing—original draft preparation, I.I., C.A. and M.K.A.; writing—review and editing, M.K.A.; supervision, C.A. All authors have read and agreed to the published version of the manuscript.

Funding: This work was funded by the EC, Environment, LIFE17 ENV/GR/000387 PureAgroH2O Programme. I. Ibrahim was financially supported by the Science Achievement Scholarship of High Education Ministry of Egypt in cooperation with the Hellenic Ministry of Foreign Affairs for his PhD Scholarship.

Institutional Review Board Statement: Not applicable.

Data Availability Statement: Data are contained within the article and Supplementary Materials.

Conflicts of Interest: The authors declare no conflicts of interest. The funders had no role in the design of the study; in the collection, analyses, or interpretation of data; in the writing of the manuscript; or in the decision to publish the results.

References

1. Pelaez, M.; Nolan, N.T.; Pillai, S.C.; Seery, M.K.; Falaras, P.; Kontos, A.G.; Dunlop, P.S.M.; Hamilton, J.W.J.; Byrne, J.A.; KO'Shea Entezari, M.H.; et al. A review on the visible light active titanium dioxide photocatalysts for environmental applications. *Appl. Catal. B* **2012**, *125*, 331–349. [\[CrossRef\]](#)
2. Theodorakopoulos, G.; Arfanis, M.K.; Pérez, J.S.; Agüera, A.; Aponte, F.X.C.; Markellou, E.; Romanos, G.; Em Falaras, P. Novel pilot-scale photocatalytic nanofiltration reactor for agricultural wastewater treatment. *Membranes* **2023**, *13*, 202. [\[CrossRef\]](#) [\[PubMed\]](#)
3. Antoniadou, M.; Falara, P.P.; Likodimos, V. Photocatalytic degradation of pharmaceuticals and organic contaminants of emerging concern using nanotubular structures. *Curr. Opin. Green Sustain. Chem.* **2021**, *29*, 100470. [\[CrossRef\]](#)
4. Wang, D.; Yin, F.X.; Cheng, B.; Xia, Y.; Yu, J.G.; Ho, W.K. Enhanced photocatalytic activity and mechanism of CeO₂ hollow spheres for tetracycline degradation. *Rare Met.* **2021**, *40*, 2369–2380. [\[CrossRef\]](#)
5. Cheng, Y.H.; Chen, J.; Che, H.N.; Ao, Y.H.; Liu, B. Ultrafast photocatalytic degradation of nitenpyram by 2D ultrathin Bi₂WO₆: Mechanism, pathways and environmental factors. *Rare Met.* **2022**, *41*, 2439–2452. [\[CrossRef\]](#)
6. Ibrahim, I.; Athanasekou, C.; Manolis, G.; Kaltzoglou, A.; Nasikas, N.K.; Katsaros, F.; Devlin, E.; Kontos, A.G.; Falaras, P. Photocatalysis as an advanced reduction process (ARP): The reduction of 4-nitrophenol using titania nanotubes-ferrite nanocomposites. *J. Hazard. Mater.* **2019**, *372*, 37–44. [\[CrossRef\]](#)
7. Liu, J.; Wang, S.L.; Xuan, J.L.; Shan, B.F.; Luo, H.; Deng, L.P.; Yang, P.; Qi, C.Z. Preparation of tungsten-iron composite oxides and application in environmental catalysis for volatile organic compounds degradation. *Tungsten* **2022**, *4*, 38–51. [\[CrossRef\]](#)
8. Ibrahim, I.; Kaltzoglou, A.; Athanasekou, C.; Katsaros, F.; Devlin, E.; Kontos, A.G.; Ioannidis, N.; Perraki, M.; Tsakiridis, P.; Sygellou, L.; et al. Magnetically separable TiO₂/CoFe₂O₄/Ag nanocomposites for the photocatalytic reduction of hexavalent chromium pollutant under UV and artificial solar light. *Chem. Eng. J.* **2020**, *381*, 122730. [\[CrossRef\]](#)
9. Zhao, M.; Zhu, X.Y.; Li, Y.Z.; Chang, J.N.; Li, M.X.; Ma, L.H.; Guo, X.Y. A Lindqvist-type [W₆O₁₉]₂ organic-inorganic compound: Synthesis, characterization, antibacterial activity and preliminary studies on the mechanism of action. *Tungsten* **2022**, *4*, 121–129. [\[CrossRef\]](#)
10. Zhang, G.; Liu, H.; Qu, J.; Li, J. Two-dimensional layered MoS₂: Rational design, properties and electrochemical applications. *Energy Environ. Sci.* **2016**, *9*, 1190. [\[CrossRef\]](#)
11. Xu, Z.; Lu, J.; Zheng, X.; Chen, B.; Luo, Y.; Tahir, M.N.; Huang, B.; Xia, X.; Pan, X. A critical review on the applications potential risks of emerging MoS₂ nanomaterials. *J. Hazard. Mater.* **2020**, *399*, 123057. [\[CrossRef\]](#)
12. Gao, Y.; Chen, C.L.; Tan, X.L.; Xu, H.; Zhu, K.R. Polyaniline-modified 3D-flower-like molybdenum disulfide composite for efficient adsorption/photocatalytic reduction of Cr(VI). *J. Colloid Interface Sci.* **2016**, *476*, 62–70. [\[CrossRef\]](#)
13. Deng, X.; Yang, Y.; Mei, Y.; Li, J.; Guo, C.; Yao, T.; Guo, Y.; Xin, B.; Wu, J. Construction of Fe₃O₄@FeS₂@C@MoS₂ Z-scheme heterojunction with sandwich-like structure: Enhanced catalytic performance in photo-Fenton reaction and mechanism insight. *J. Alloys Compd.* **2022**, *901*, 163437. [\[CrossRef\]](#)
14. Zhang, Y.; Chen, P.; Wen, F.; Meng, Y.; Yuan, B.; Wang, H. Synthesis of S-rich flower-like Fe₂O₃-MoS₂ for Cr(VI) removal. *Sep. Sci. Technol.* **2016**, *11*, 1779–1786. [\[CrossRef\]](#)
15. Tao, Q.; Bi, J.; Huang, X.; Wei, R.; Wang, T.; Zhou, Y.; Hao, H. Fabrication, application, optimization and working mechanism of Fe₂O₃ and its composites for contaminants elimination from wastewater. *Chemosphere* **2021**, *263*, 127889. [\[CrossRef\]](#) [\[PubMed\]](#)
16. Mishra, M.; Chun, D.M. α -Fe₂O₃ as a photocatalytic material: A review. *Appl. Catal. A Gen.* **2015**, *498*, 126–141. [\[CrossRef\]](#)
17. Li, J.; You, J.; Wang, Z.; Zhao, Y.; Xu, J.; Li, X.; Zhang, H. Application of α -Fe_{1-x}O₃-based heterogeneous photo-Fenton catalyst in wastewater treatment: A review of recent advances. *J. Environ. Chem. Eng.* **2022**, *10*, 108329. [\[CrossRef\]](#)
18. Yang, X.; Sun, H.; Zhang, L.; Zhao, L.; Lian, J.; Jiang, Q.; Cong, Y. High Efficient Photo-Fenton Catalyst of α -Fe₂O₃/MoS₂ Hierarchical Nanoheterostructures: Reutilization for Supercapacitors. *Sci. Rep.* **2016**, *6*, 31591. [\[CrossRef\]](#) [\[PubMed\]](#)

19. Zhang, T.; Zhang, H.; Ji, Y.; Chi, N.; Cong, Y. Preparation of a novel Fe₂O₃-MoS₂-CdS ternary composite film and its photoelectrocatalytic performance. *Electrochim. Acta* **2018**, *285*, 230–240. [[CrossRef](#)]
20. Cong, Y.; Ding, W.; Zhang, W.; Zhang, T.; Wang, Q.; Zhang, Y. Fabrication of a novel 3D E-Fe₂O₃-Pi-MoS₂ film with highly enhanced carrier mobility and photoelectrocatalytic activity. *Electrochim. Acta* **2020**, *337*, 135748. [[CrossRef](#)]
21. Li, A.; Liu, Y.; Xu, X.; Zhang, Y.; Si, Z.; Wu, X.; Ran, R.; Weng, D. MOF-derived (MoS₂, g-Fe₂O₃)/graphene Z-scheme photocatalysts with excellent activity for oxygen evolution under visible light irradiation. *RSC Adv.* **2020**, *10*, 17154. [[CrossRef](#)]
22. Tama, A.M.; Das, S.; Dutta, S.; Bhuyan, M.D.I.; Islam, M.N.; Basith, M.A. MoS₂ nanosheet incorporated α -Fe₂O₃/ZnO nanocomposite with enhanced photocatalytic dye degradation and hydrogen production ability. *RSC Adv.* **2019**, *9*, 40357–40367. [[CrossRef](#)]
23. Zhao, Y.; Cai, W.; Shi, Y.; Tang, J.; Gong, Y.; Chen, M.; Zhong, Q. Construction of Nano-Fe₂O₃-Decorated Flower-Like MoS₂ with Fe-S Bonds for Efficient Photoreduction of CO₂ under Visible-Light Irradiation. *ACS Sustain. Chem. Eng.* **2020**, *8*, 12603–12611. [[CrossRef](#)]
24. Khabiri, G.; Aboraia, A.M.; Soliman, M.; Guda, A.A.; Butova, V.V.; Yahia, I.S.; Soldatov, A.V. A novel α -Fe₂O₃@MoS₂ QDs heterostructure for enhanced visible-light photocatalytic performance using ultrasonication approach. *Ceram. Int.* **2020**, *46*, 19600–19608. [[CrossRef](#)]
25. Mu, D.; Chen, Z.; Shi, H.; Tan, N. Construction of flower-like MoS₂/Fe₃O₄/rGO composite with enhanced photo-Fenton like catalyst performance. *RSC Adv.* **2018**, *8*, 36625–36631. [[CrossRef](#)]
26. Wang, H.; Li, X.; Ge, Q.; Chong, Y.; Zhang, Y. A multifunctional Fe₂O₃@MoS₂@SDS Z-scheme nanocomposite: NIR enhanced bacterial inactivation, degradation antibiotics and inhibiting ARGs dissemination. *Colloids Surf. B* **2022**, *219*, 112833. [[CrossRef](#)]
27. Ibrahim, I.; Ali, I.O.; Salama, T.M.; Bahgat, A.A.; Mohamed, M.M. Synthesis of magnetically recyclable spinel ferrite (MFe₂O₄, M = Zn, Co, Mn) nanocrystals engineered by sol gel-hydrothermal technology: High catalytic performances for nitroarenes reduction. *Appl. Catal. B-Environ.* **2016**, *181*, 389–402. [[CrossRef](#)]
28. Mohammadpour, E.; Asadpour-Zeynali, K. α -Fe₂O₃@MoS₂ nanostructure as an efficient electrochemical catalyst for water oxidation. *Microchem. J.* **2020**, *157*, 104939. [[CrossRef](#)]
29. Falara, P.P.; Ibrahim, I.; Zourou, A.; Sygellou, L.; Sanchez, D.E.; Romanos, G.; Em Givalou, L.; Antoniadou, M.; Arfanis, M.K.; Han, C.; et al. Bi-functional photocatalytic heterostructures combining titania thin films with carbon quantum dots (C-QDs/TiO₂) for effective elimination of water pollutants. *Environ. Sci. Pollut. Res.* **2023**, *30*, 124976–124991. [[CrossRef](#)]
30. Reddy, D.A.; Park, H.; Hong, S.; Kumar, D.P.; Kim, T.K. Hydrazine-assisted formation of ultrathin MoS₂ nanosheets for enhancing their co-catalytic activity in photocatalytic hydrogen evolution. *J. Mater. Chem. A* **2017**, *5*, 6981–6991. [[CrossRef](#)]
31. Luo, R.; Xu, W.W.; Zhang, Y.; Wang, Z.; Wang, X.; Gao, Y.; Liu, P.; Chen, M. Van der Waals interfacial reconstruction in monolayer transition-metal dichalcogenides and gold heterojunctions. *Nat. Commun.* **2020**, *11*, 1011. [[CrossRef](#)] [[PubMed](#)]
32. Blanco, E.; Afanasiev, P.; Berhault, G.; Uzio, D.; Loridan, S. Resonance Raman spectroscopy as a probe of the crystallite size of MoS₂ nanoparticles. *Comptes Rendus Chim.* **2016**, *19*, 1310–1314. [[CrossRef](#)]
33. Yao, Y.; Ao, K.; Lv, P.; Wei, Q. MoS₂ Coexisting in 1T and 2H Phases Synthesized by Common Hydrothermal Method for Hydrogen Evolution Reaction. *Nanomaterials* **2019**, *9*, 844. [[CrossRef](#)] [[PubMed](#)]
34. Marshall, C.P.; Dufresne, W.J.B.; Ruffledt, C.J. Polarized Raman spectra of hematite assignment of external modes. *J. Raman Spectrosc.* **2020**, *51*, 1522–1529. [[CrossRef](#)]
35. Wei, F.; Cui, X.; Wang, Z.; Dong, C.; Li, J.; Han, X. Recoverable peroxidase-like Fe₃O₄@MoS₂-Ag nanozyme with enhanced antibacterial ability. *Chem. Eng. J.* **2021**, *408*, 127240. [[CrossRef](#)] [[PubMed](#)]
36. Khawula, T.N.Y.; Raju, K.; Franklyn, P.J.; Sigalas, I.; Ozoemena, K.I. Symmetric pseudocapacitors based on molybdenum disulfide (MoS₂)-modified carbon nanospheres: Correlating physicochemistry synergistic interaction on energy storage. *J. Mater. Chem. A* **2016**, *4*, 6411. [[CrossRef](#)]
37. Theerthagiri, J.; Senthil, R.A.; Priya, A.; Madhavan, J.; Michael, R.J.V.; Ashokkumar, M. Photocatalytic and photoelectrochemical studies of visible-light active α -Fe₂O₃-g-C₃N₄ nanocomposites. *RSC Adv.* **2014**, *4*, 38222–38229. [[CrossRef](#)]
38. Saha, N.; Sarkar, A.; Ghosh, A.B.; Dutta, A.K.; Bhadu, G.R.; Parimal, P.; Adhikary, B. Highly active spherical amorphous MoS₂: Facile synthesis and application in photocatalytic degradation of rose bengal dye and hydrogenation of nitroarenes. *RSC Adv.* **2015**, *5*, 88848–88856. [[CrossRef](#)]
39. Cai, J.; Li, S.; Pan, H.; Liu, Y.; Qin, G. c-In₂O₃/α-Fe₂O₃ heterojunction photoanodes for water oxidation. *J. Mater. Sci.* **2016**, *51*, 8148–8155. [[CrossRef](#)]
40. Yang, Y.; Wang, Q.; Zhang, X.; Deng, X.; Guan, Y.; Wu, M.; Liu, L.; Wu, J.; Yao, T.; Yin, Y. Photocatalytic generation of H₂O₂ over a Z-scheme Fe₂O₃@C@1T/2H-MoS₂ heterostructured catalyst for high-performance Fenton reaction. *J. Mater. Chem. A* **2023**, *11*, 1991. [[CrossRef](#)]

Disclaimer/Publisher's Note: The statements, opinions and data contained in all publications are solely those of the individual author(s) and contributor(s) and not of MDPI and/or the editor(s). MDPI and/or the editor(s) disclaim responsibility for any injury to people or property resulting from any ideas, methods, instructions or products referred to in the content.